Letters

Constant Frequency CC–CV Operation of Isolated *LLC* Resonant DC-DC Converter Using Switched Capacitor Network for WCS

Kirshan Kumar Gautam, Amitabh Chatterjee, Subhendu Bikash Santra, *Senior Member, IEEE*, and Dinkar Prasad

***Abstract*—In this letter a new circuit structure based on *LLC* resonant isolated dc-dc converter is proposed to achieve constant current-constant voltage (CC–CV) characteristics for wireless charging system (WCS). Complex reconfigurable network-based *LLC* resonant dc-dc converter can provide CC–CV at a constant switching frequency. This work is an alternative solution based on fixed isolated *LLC* resonant dc-dc circuit where extra capacitor switch arrangement is used to achieve CC–CV characteristics at a constant switching frequency with seamless transition feature. All inverter switches are soft switched throughout CC–CV operation. In addition, the kVA/kW optimization method is employed to reduce reactive component sizing for achieving high power density. A 600 W prototype with an average kVA/kW ratio of 30 and a peak efficiency of 96% at a coupling coefficient of 0.2 has been designed to validate the proposed WCS.**

***Index Terms*—Constant voltage–constant current (CC–CV) characteristics, wireless charging system (WCS).**

I. Introduction

WIRELESS power transfer (WPT) is an emerging technology that provides manifold advantages over traditional charging methods in various fields such as electric vehicles (EVs) charging, bio-medical implants, LED lighting systems, etc. [1], [2]. Wireless charging system (WCS) is one of the applications of WPT technology. Li-ion batteries for EV require constant current (CC)–constant voltage (CV) charging [3] to achieve longer battery lifespan. WCS has high leakage inductance and requires large magnetizing current at power frequency. Therefore, power electronics (PE) converters for WCS requires CC–CV mode, compensation network, and lower magnetizing current. In the last decade, isolated *LLC* resonant dc-dc converter as shown in Fig. 1 is extensively studied for WCS system-more specifically on CC–CV characteristics [4], [5].

Variable switching frequency operation (wider range) with compensating network is essential for achieving CC–CV for WCS [6], [7]. It leads to increased switching losses and VA ratings. Furthermore, these control approaches are complex and frequency tuning may violate certain standard such as J2954 from the society of automotive engineers [8]. Modifications in the fundamental isolated *LLC* resonant dc-dc converter circuit are tried using additional dc-dc converter [9], [10], modification in pulse width modulation (PWM) strategy [11], and three-coil structure [12], [13] to achieve CC–CV output at constant frequency (CF). However, performance parameters such as efficiency, operation complexity, and volume are discouraging. Reconfigurable topologies [14], [15], [16] offer another approach as mentioned in Fig. 1 to achieve CC–CV output at CF. However, it suffers from a high component count, including many switches, capacitors, receiver coils, which increases complexity, cost, and size of WCS. Another problem is high voltage spikes (larger voltage stress) due to interrupting inductor current.

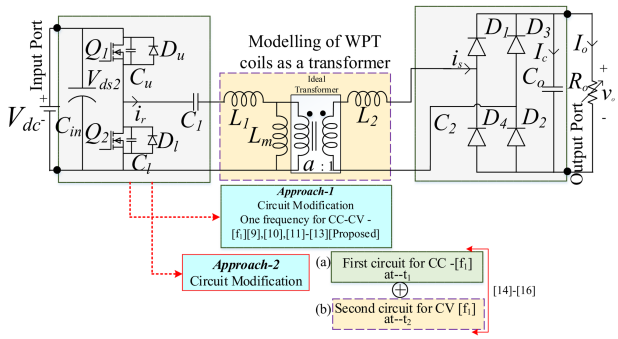

Fig. 1. Isolated *LLC* resonant DC-DC converter structure for WCS.

In this work a novel switched capacitor (SC)-based resonant tank circuit is proposed on fixed isolated *LLC* resonant converter to produce CC–CV output at CF. The proposed system is extremely simple, requiring only two switches and SC network for achieving capacitance variation which changes resonant frequency position. Transition between CC and CV charging modes is smooth in proposed configuration, which eliminates complex topological changes. It only requires two additional SC networks in primary and secondary coils in WCS.

II. Proposed Reconfigurable WCS for CC–CV Output

The proposed SC-based *LLC* resonant dc-dc converter which provides CC-CV output at fixed frequency is shown in Fig. 2.

Received 8 June 2024; revised 10 August 2024; accepted 25 August 2024. Date of publication 3 September 2024; date of current version 12 December 2024. *(Corresponding author: Kirshan Kumar Gautam.)*

The authors are with the Department of Electrical Engineering, Shiv Nadar Institution of Eminence Deemed to be University, Delhi-NCR 201314, India (e-mail: kg982@snu.edu.in; amitabh.chatterjee@snu.edu.in; subhendu.santra@snu.edu.in; dinkar.prasad@snu.edu.in).

Color versions of one or more figures in this article are available at https://doi.org/10.1109/TPEL.2024.3453512.

Digital Object Identifier 10.1109/TPEL.2024.3453512

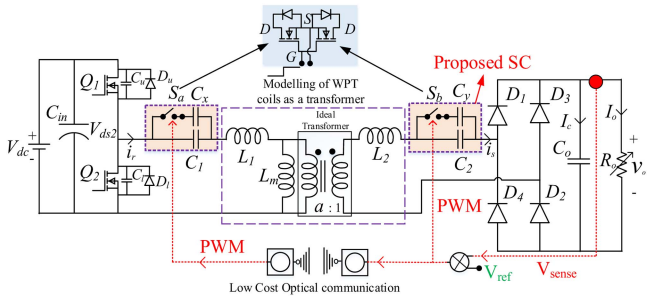

Fig. 2. Proposed SC-based converter for CC–CV at fixed PWM frequency.

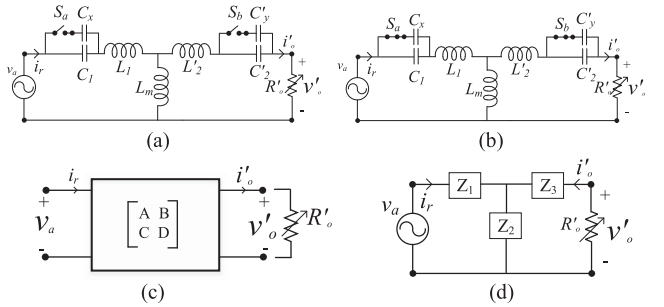

Fig. 3. AC equivalent circuit of the proposed WCS. (a) CC charging mode. (b) CV charging mode. (c) ABCD parameters of converter. (d) Two port representation of proposed WCS.

The circuit includes the leakage inductances (L_1 and L_2) of both side coils. Compensation capacitors C_1 and C_2 are connected in series with their corresponding windings to mitigate the effects of these leakage inductances and achieve resonance at the desired operating frequency. The magnetizing inductance (L_M) signifies the mutual coupling between the transmitter and receiver coils. To ensure seamless transitions between CC and CV modes, an SC network with two ac switches (S_a and S_b) is incorporated. When S_a and S_b are deactivated, capacitors C_1 and C_2 make a specific frequency for CC mode operation. Conversely, when S_a and S_b are activated, then external compensation capacitors (C_x and C_y) are added in parallel with C_1 and C_2. This makes changes in circuit's resonant frequency, which enables CV mode. This mode change is preciously designed based on SC network values, which is proved through ABCD parameter analysis and practical network analyzer-based impedance data.

A. Analysis of CC–CV Operation Using ABCD Parameter

The ac equivalent circuit of the proposed WCS referred to the transmitter side is shown in Fig. 3.

Using the first harmonic approximation method, transmitter side reflected load resistance (R'_o), half-bridge inverter's output voltage (v_o) and rms voltage of fundamental output (v_a) are defined as follows:

$$R_o{}' = \frac{v'_o}{i'_o} = \frac{8n^2 R_o}{\pi^2},\ v_0 = \sum_{1,3,5}^{\infty} \frac{2V_{\rm dc}}{n\pi}\sin(n\omega t),\ v_a = \frac{\sqrt{2}V_{\rm dc}}{\pi} \Bigg\} \quad (1)$$

where load resistance $R_o = V_o/I_o$. The AC equivalent circuit again can be represented in two port parameters [ABCD], as shown in Fig. 3(c) and (d), which identifies the CC–CV operation at different resonant frequencies.

$$\begin{bmatrix} v_a \\ i_r \end{bmatrix} = \begin{bmatrix} A & B \\ C & D \end{bmatrix} \begin{bmatrix} v'_o \\ -i'_o \end{bmatrix}. \quad (2)$$

The voltages and currents at the input and output ports of a two-port network represented by v_a, i_r, and v'_o, i'_o, respectively. The ABCD parameter of the proposed converter is given as follows:

$$\begin{bmatrix} v_a \\ i_r \end{bmatrix} = \begin{bmatrix} \frac{Z_1+Z_2}{Z_2} & \frac{(Z_1+Z_2)(Z_2+Z_3)-Z_2^2}{Z_2} \\ \frac{1}{Z_2} & \frac{Z_2+Z_3}{Z_2} \end{bmatrix} \begin{bmatrix} v'_o \\ -i'_o \end{bmatrix} \quad (3)$$

where, $Z_1 = j\omega L_1 + \frac{1}{j\omega C_1}$, $Z_2 = j\omega L_m$, and $Z_3 = j\omega L'_2 + \frac{1}{j\omega C'_2}$ in CC, whereas in CV, $Z_1 = j\omega L_1 + \frac{1}{j\omega(C_1+C_x)}$, $Z_2 = j\omega L_m$, and $Z_3 = j\omega L'_2 + \frac{1}{j\omega(C'_2+C'_y)}$. By comparing (2) and (3), ABCD parameters of the proposed WCS can be found out. Condition for constant current (CC) and constant voltage (CV) can be derived by (4) and (5), respectively, as follows:

$$\begin{bmatrix} v_a \\ i_r \end{bmatrix} = \begin{bmatrix} 0 & B \\ C & 0 \end{bmatrix} \begin{bmatrix} v'_o \\ -i'_o \end{bmatrix} \quad (4)$$

$$\begin{bmatrix} v_a \\ i_r \end{bmatrix} = \begin{bmatrix} A & 0 \\ C & D \end{bmatrix} \begin{bmatrix} v'_o \\ -i'_o \end{bmatrix}. \quad (5)$$

From (3) and (4) operating frequency can be derived for CC output by putting condition $Z_1 + Z_2 = Z_2 + Z_3 = 0$.

$$f_{01,(\rm CC)} = \frac{1}{2\pi\sqrt{(L_1+L_m)C_1}} = \frac{1}{2\pi\sqrt{(L_2+L_m)C_2}}. \quad (6)$$

The ABCD parameters of WCS at $f_{o1,(\rm CC)}$ for CC output given as follows:

$$\begin{bmatrix} v_a \\ i_r \end{bmatrix} = \begin{bmatrix} 0 & -Z_2 \\ \frac{1}{Z_2} & 0 \end{bmatrix} \begin{bmatrix} v'_o \\ -i'_o \end{bmatrix}. \quad (7)$$

Again, comparing (3) and (5) operating frequency can be derived for CV output, by putting condition $Z_1 = Z_3 = 0$.

$$f_{0,(\rm CV)} = \frac{1}{2\pi\sqrt{L_1(C_1+C_x)}} = \frac{1}{2\pi\sqrt{L_2(C_2+C_y)}}. \quad (8)$$

The ABCD parameters of converter at $f_{o,(\rm CV)}$ for CV output given as follows:

$$\begin{bmatrix} v_a \\ i_r \end{bmatrix} = \begin{bmatrix} 1 & 0 \\ \frac{1}{Z_2} & 1 \end{bmatrix} \begin{bmatrix} v'_o \\ -i'_o \end{bmatrix}. \quad (9)$$

Condition for a current source is that its Norton equivalent impedance (Z_n) will be equal to infinity. The output impedance of the proposed converter is tested practically using a hardware set up as shown in Fig. 4(a). The measurement circuit for CC and CV mode are also shown in Fig. 4(b) and (c), respectively. From measurement, CC characteristics are found at $f_{o1,(\rm CC)}$, i.e., 114.7 kHz as shown in Fig. 4(d). Similarly, at resonant frequency ($f_{o,(\rm CV)}$), i.e., 114.3 kHz shows CV operation, which is shown in Fig. 4(e). This measurement is important as it guides

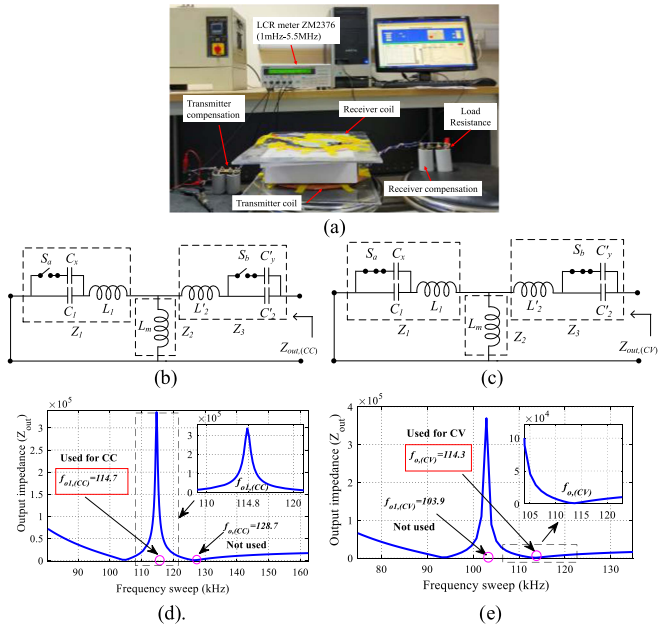

Fig. 4. (a) Output impedance (Z_{out}) measurement set up. (b) Measurement circuit in CC mode. (c) Measurement circuit in CV mode. (d) Experimental output impedance in CC mode. (e) Experimental output impedance in CV mode.

selection of accurate SC network values, which confirms CC–CV changeover at constant switching frequency. Thus, $f_{o1,(\mathrm{CC})}$ is equal to $f_{o,(\mathrm{CV})}$.

$$f_{o1,(\mathrm{CC})} = f_{o(\mathrm{CV})}. \tag{10}$$

B. Current and Voltage Gain in CC–CV Mode

For simplifying gain in CC–CV mode of proposed converter normalization of frequency and impedances are essential where the base frequency and base impedance are ω_o and Z_o, respectively. Quality factor (Q), normalized switching frequency (f_n or ω_n), ratio from magnetizing inductance to leakage inductance (φ) is defined as follows:

$$\left.\begin{aligned} \omega_o = \frac{1}{\sqrt{L_1C_1}} &= \frac{1}{\sqrt{L_2C_2}}, Q = \frac{Z_o}{R'_o} \\ \omega_n = f_n = \frac{\omega_s}{\omega_o} &= \frac{f_s}{f_o}, \; Z_o = \sqrt{\frac{L_1}{C_1}}, \varphi = \frac{L_m}{L_1} = \frac{k}{1-k} \end{aligned}\right\}. \tag{11}$$

The equivalent input impedance (Z_{in}) and the normalized input impedance ($Z_n = Z_{\mathrm{in}}/Z_o$) are obtained as follows:

$$Z_{\mathrm{in}} = Z_1 + [Z_2 || (Z_3 + R'_o)]. \tag{12}$$

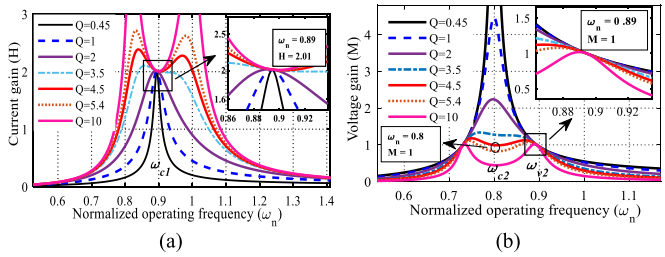

Fig. 5. (a) Current gain in CC mode. (b) Voltage gain in CV mode.

The voltage gain (M) and current gain (H) can be expressed as follows:

$$M = \frac{v'_o}{v_a} \text{ and } H = \frac{i'_o}{\frac{v_{dc}}{Z_o}} = \frac{\sqrt{2}}{\pi} MQ. \tag{13}$$

Where $M = \frac{v'_o}{v_a} = \left| \left(\frac{Z_2 || (Z_3 + R'_o)}{Z_1 + [Z_2 || (Z_3 + R'_o)]} \right) \left(\frac{R'_o}{Z_3 + R'_o} \right) \right|$. Equation (14) shown at the bottom of this page.

The current gain remains constant regardless of the load (Q) when the system operated at $f_{o1,(\mathrm{CC})}$, as shown in Fig. 5(a).

$$\omega_n = \omega_{c1} = \frac{1}{\sqrt{1+\varphi}} = \sqrt{1-k} \tag{15}$$

where ω_{c1} is the normalized operating frequency and current gain H at ω_{c1} is given as follows:

$$H_{\omega_n = \omega_{c1}} = \frac{\sqrt{2}}{\pi} \frac{\sqrt{1+\varphi}}{\varphi} = \frac{\sqrt{2}}{\pi} \frac{\sqrt{1-k}}{k}. \tag{16}$$

In CV mode, switches S_a and S_b are closed, and the resonant tank is now composed of L_l, L_m, L_2, $(C_1 + C_x)$, and $(C_2 + C_y)$. Hence, new series resonant frequency is $f_{o,(\mathrm{CV})}$. Fig. 5(b) shows the M characteristics of the converter. When the system operates at $f_{o,(\mathrm{CV})}$ or $\omega_n = \omega_{v2}$, the voltage gain remains constant regardless of the load (Q), where ω_{v2} is the new normalized series operating frequency and M is independent of the load. From Fig. 5(a) and (b) it is concluded that the M and H gain curves independent to the load at the normalized frequency ($\omega_n = \omega_{c1} = \omega_{v2} = 0.89$) it will show the CF operation in both CC and CV modes.

The frequencies ω_{c1} and ω_{v2} are the normalized operating frequency for achieving CC and CV output in CC mode (when S_a and S_b are open) and in CV mode (when S_a and S_b are closed), respectively.

The phase of normalized input impedance (θ) between the input voltage and input current are obtained as follows:

$$M(\omega) = \left[\frac{\begin{array}{c} \frac{\omega_n^{10}\varphi}{Q^2}(1+\varphi) + \frac{\omega_n^8}{Q^2}\left(\frac{1+\varphi}{Q^2} - 2\varphi - 3\right) + \frac{\omega_n^6\varphi}{Q^2}\left(3 + \varphi - \frac{1}{Q^2}\right) - \frac{\omega_n^4\varphi}{Q^2} \\ +j\left(-\frac{\omega_n^{11}\varphi}{Q}(1+2\varphi) + \frac{\omega_n^9\varphi}{Q}\left(4 + 6\varphi - \frac{1+2\varphi}{Q^2}\right) + \frac{\omega_n^7\varphi}{Q}\left(\frac{2+2\varphi}{Q^2} - 6 - 6\varphi\right)\right. \\ \left. + \frac{\omega_n^5\varphi}{Q}\left(4 + 2\varphi - \frac{1}{Q^2}\right) - \frac{\omega_n^3\varphi}{Q}\right) \end{array}}{\begin{array}{c} \left[1 - \omega_n^2\left(3 + 2\varphi + \frac{1}{Q^2}\right) + \omega_n^4\left(3 + 4\varphi + \frac{1+\varphi}{Q^2}\right) - \omega_n^6(1+2\varphi)\right]^2 \\ + \left[\frac{\omega_n^5}{Q}(2+3\varphi) - \frac{\omega_n^3}{Q}(4+3\varphi) + \frac{2\omega_n}{Q}\right]^2 \end{array}} \right]. \tag{14}$$

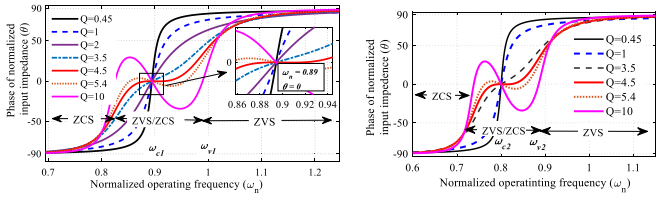

Fig. 6. Input phase (θ) of the Z_n. (a) CC mode. (b) CV mode.

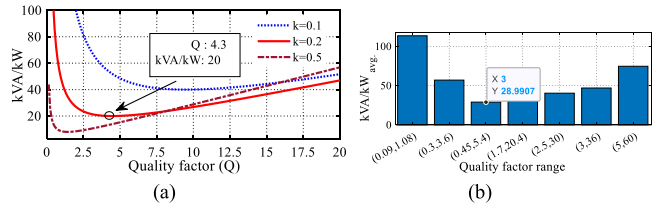

Fig. 7. (a) kVA/kW rating by varying Q with different coupling. (b) Average kVA/kW rating with coupling factor (k) = 0.2.

Using (17) shown at the bottom of this page, ω_n versus θ of Z_n is plotted in Fig. 6 for different values of "Q" in both CC and CV mode. The θ equal to zero at ω_n equal to ω_{c1} given as follows:

$$\theta \mid_{\omega_n=\omega_{c1}} = 0. \tag{18}$$

Fig. 6(a) shows zero power angle at ω_{c1} (in CC mode) resulting zero voltage switching (ZVS) at turn-ON and zero current switching (ZCS) at turn-OFF operation. Similarly, in Fig. 6(b) the θ is greater than zero by setting ω_n equal to ω_{v2} (in CV mode) shows inductive nature of the circuit, which confirms the ZVS turn-ON operation.

III. kVA/kW Design Optimization

kVA/kW-based design optimization is used to determine the physical size of the converter, which reduces size of reactive components. The kVA/kW of proposed WCS is given as (19) shown at the bottom of this page.

The normalized rms current and voltages are calculated as follows:

$$I_{qn} = \frac{I_{q,\text{rms}}}{V_{\text{dc}}/Z_o}\ ,\ V_{qn} = \frac{V_{q,\text{rms}}}{V_{\text{dc}}} \tag{20}$$

where q is the respective component, the base voltage and base current is taken as V_{dc} and (V_{dc} /Z_o), respectively. Fig. 7(a) shows the plot of (22) as a function of Q and k. The battery resistance (R_o) varies in the range of 5 to 60 Ω from start of CC mode to end of CV mode. The Q factor as defined in (11) has R'_o (= 8 n^2 R_o/π^2) term in the denominator. Thus, a change in R_o from 5 Ω to 60 Ω results in a change in Q from 5.4 to 0.45 (i.e., a change by a factor of 0.083).

TABLE I
Design Parameters of the Prototype

C_1	C_2	C_x	C_y	L_p	L_s	k	n
16.59 nF	51.4 nF	4.08 nF	12.5 nF	113.41 μH	34.1 μH	0.195	1.81

$$\left.\begin{aligned}
&Z_n \mid_{\omega_n=\omega_c} = \frac{Q\varphi^2}{1+\varphi}, M \mid_{\omega_n=\omega_c} = \frac{\sqrt{1+\varphi}}{\varphi Q}, H \mid_{\omega_n=\omega_c} = \frac{\sqrt{2}}{\pi}\frac{\sqrt{1+\varphi}}{\varphi}\\
&|I_{L_1n}| = \frac{\sqrt{2}}{\pi}\left(\frac{1+\varphi}{Q\varphi^2}\right), |V_{L_1n}| = \frac{\sqrt{2}}{\pi}\left(\frac{\sqrt{1+\varphi}}{Q\varphi^2}\right), |V_{C_1n}| = \frac{\sqrt{2}}{\pi}\left(\frac{(1+\varphi)^{\frac{3}{2}}}{Q\varphi^2}\right)\\
&|I_{mn}| = \frac{\sqrt{2}}{\pi}\frac{\sqrt{((1+\varphi)-Q^2\varphi^2)}}{Q\varphi}, |V_{mn}| = \frac{\sqrt{2}}{\pi}\frac{\sqrt{1+\varphi}\sqrt{(Q\varphi)^2+\varphi+1}}{Q\varphi^2}\\
&\left|I_{L'_{2n}}\right| = \frac{\sqrt{2}\sqrt{1+\varphi}}{\pi\varphi}, \left|V_{L'_{2n}}\right| = \frac{\sqrt{2}}{\pi\varphi}, \left|V_{C'_{2n}}\right| = \frac{\sqrt{2}(1+\varphi)}{\pi\varphi}
\end{aligned}\right\}. \tag{21}$$

$$\frac{\text{kVA}}{\text{kW}} = \frac{\pi}{\sqrt{2}}\frac{\left(\begin{matrix}2+3\varphi+\varphi^2+2Q^2\varphi^2+Q^2\varphi^3\\ +\varphi^7\sqrt{1+\varphi-Q^2\varphi^2}\sqrt{1+\varphi+Q^2\varphi}\end{matrix}\right)}{Q\varphi^2\sqrt{1+\varphi}}. \tag{22}$$

$$\text{kVA/k W}_{\text{Avg}} = \frac{1}{\Delta Q}\int_{Q_x}^{Q_y}\frac{\text{kVA}}{\text{kW}}dQ. \tag{23}$$

Fig. 7(b) shows the plots of (23), which indicate the average kVA/kW rating within the entire charging cycle of the battery. For the range of Q, 0.45 to 5.4, the average value of kVA/kW rating is almost minimum, and the corresponding size is also minimum. Therefore, by using an optimum Q range (0.45, 5.4), the minimum size is found at $k = 0.2$.

After examining (14), it has been concluded that the voltage gain is unity for $Q = 4.5$ and $k = 0.2$ at both $\omega_n = \omega_{c2}$ and at $\omega_n = \omega_{v2}$, as shown in Fig. 5(b). Using this value of Q = 4.5 the designed parameters of the proposed WCS are calculated using (24) and it is mentioned in Table I. Where L_p is the self-inductance (sum of leakage and mutual inductances) of transmitter side winding and L_s is for receiver side winding. "n" denotes the primary to secondary windings' turns-ratio. It

$$\theta = \tan^{-1}\left(\frac{Q\left(\omega_n^6\left(1+3\varphi+2\varphi^2\right)-\omega_n^4\left(3+6\varphi+2\varphi^2-\frac{1+\varphi}{Q^2}\right)+\omega_n^2\left(3+3\varphi-\frac{1}{Q^2}\right)-1\right)}{\omega_n^5\varphi^2}\right). \tag{17}$$

$$\frac{\text{kVA}}{\text{kW}} = \frac{|I_{L_1n}|\left(|V_{L_1n}|+|V_{C_1n}|\right)+|I_{mn}||V_{L_mn}|+\left|I_{L'_{2n}}\right|\left(\left|V_{L'_2}n\right|+\left|V_{C'_2}n\right|\right)}{\frac{2}{\pi^2}|M|^2Q}. \tag{19}$$

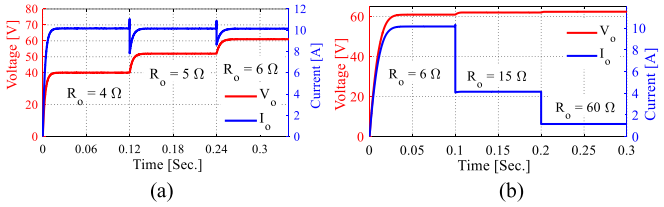

Fig. 8. Simulation results of V_o and I_o. (a) CC mode transient operation. (b) CV mode transient operation.

may be noted that $L_p = n^2 L_s$ (within allowable truncation error).

$$\left.\begin{aligned} n &= \frac{\sqrt{2}|M|_{\omega=\omega_v} V_{\rm dc}}{\pi(V_o)},\ C_1 = \frac{1}{\omega_o^2(L_1+L_m)},\ L_1 = \frac{QR'_o}{\omega_o},\\ L_m &= \frac{k}{1-k}\ L_1\\ C_2 &= \frac{1}{\omega_o^2(L_2+L_m)},\ L_2 = n^2\ L_1,\ L_p = \frac{1}{1-k}\ L_1,\ L_s = \frac{1}{1-k}\ L_2\\ C_x &= \frac{1}{4\pi^2 L_1 f_{01,(CC)}^2} - C_1,\ C_y = \frac{1}{4\pi^2 f_{01,(CC)}^2 L_2} - C_2 \end{aligned}\right\}. \tag{24}$$

IV. Simulation and Experimental Results

In total, 600 W (60 V/10 A) prototype is designed and operated at fixed switching frequency (115.6 kHz) which is closer to theoretical and practical impedance measurement, i.e., 114.7 kHz to get CC–CV operation. Simulated waveforms of the output voltage (V_o) and output current (I_o) under varying load conditions for CC and CV charging modes are shown in Fig. 8(a) and (b), respectively.

The Silicon Carbide (SiC) MOSFETs (NVH4L075N065SC1) are employed as switches Q_1 *and* Q_2. Later, GaN transistors (IGT60R070D1) are also used for comparison. High frequency polypropylene capacitors are used as C_1, C_2, C_x, and C_y. Due to several merits circular charging coils are extensively utilized for charging applications. Schottky fast diodes (STPS80H100CWLY) are used as D_1 to D_4.

The key waveform with $R_o = 6\,\Omega$ in CC and in CV charging at steady state condition are shown in Fig. 9(a) and (b), respectively. Fig. 9(c) shows that the converter maintains constant output current at 10 A, and zero power angle (ZPA) condition. This ensures advantage of both ZVS turn-ON and ZCS turn-OFF while R_o changes from 1.2 to 6 Ω. Similarly, Fig. 9(d) demonstrates stable output voltage 60 V under varying load resistance (6 to 30 Ω) and i_r is observed to lag behind V_{ds2}, achieving ZVS at turn-ON.

The ZVS turn-ON result for switch Q_2 is shown in Fig. 10(a). Similar soft-switching characteristics are also observed for switch Q_1. In Fig. 10(a), V_{ds2} represents the drain-to-source voltage of Q_2, while I_{d2} represents the drain current. V_{gs2} is the gate-to-source voltage (control signal) of MOSFET Q_2. It can be observed that the antiparallel diode of Q_2 is turned ON before Q_2 conducts and ZVS performance closely matches with simulation. Fig. 10(b) shows the voltages of the compensation capacitors during the CC–CV transition. Also, the seamless transition from CC to CV mode is shown in Fig. 11. Throughout this transition, the system consistently upholds a stable voltage

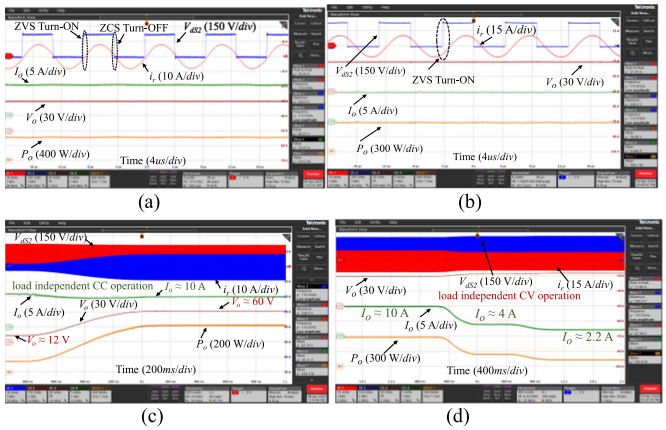

Fig. 9. Experimental waveforms of the V_{ds2}, i_r, V_o, I_o, and P_o in steady state and transient condition. (a) Steady CC charging. (b) Steady CV charging. (c) Transient CC (R_o varies from 1.2 Ω to 6 Ω). (d) Transient CV (R_o varies from 6 Ω to 30 Ω).

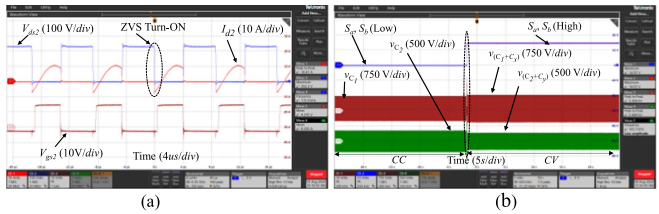

Fig. 10. (a) Experimental waveforms of V_{ds2}, I_{d2}, and v_{gs2}, in CV charging at rated load power. (b) Experimental waveforms of compensating capacitors voltage during CC–CV transition.

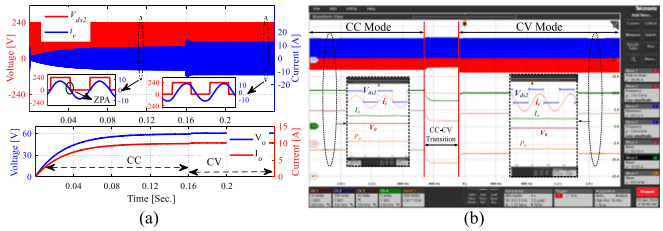

Fig. 11. Transition from CC to CV mode. (a) Simulated. (b) Experimental.

of 60 V. However, during CV charging, there is an increase in reactive power consumption, leading to an increase in i_r. As a result, compared to CC charging, CV charging has somewhat lower efficiency.

The impact of misalignment on power transfer is also studied for CC mode and CV mode. Fig. 12(a) and (b) show a plot of experimentally obtained output power for different misalignment distance in both CC and CV charging modes, respectively. In CC charging, at a misalignment of 5.3 cm resulting in an increase of P_o from 600 to 898.3 W, while the resonant frequency $f_{o1,(CC)}$ remains unaffected. In CC mode, the switching frequency is same as the resonant frequency of compensation capacitor and self-inductance of coil. As a result, the circuit continues to function under ZPA conditions even when misaligned, as illustrated in Fig. 13(a).

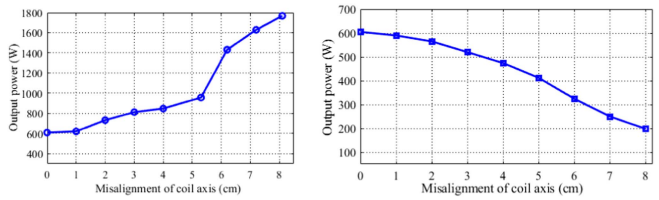

Fig. 12. Output power (P_o) versus misalignment distance. (a) In CC mode. (b) In CV mode.

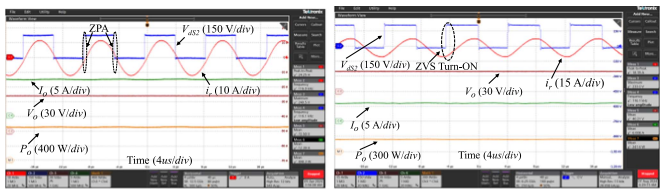

Fig. 13. Experimental waveforms of the V_{ds2}, i_r, V_o, I_o, and P_o in misaligned condition ($\Delta = 5.3$ cm). (a) In CC mode. (b) In CV mode.

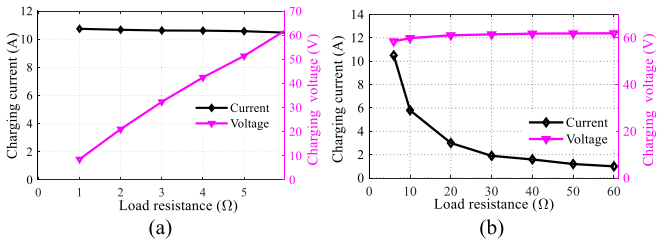

Fig. 14. Experimental results of V_o and I_o with change in R_o. (a) In CC mode. (b) In CV mode.

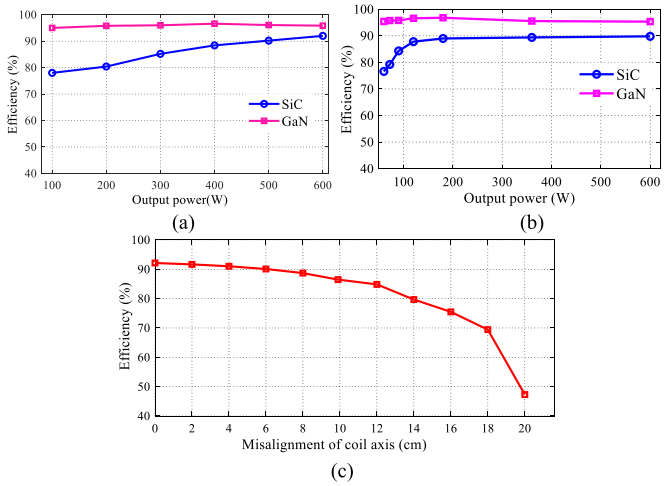

Fig. 15. Experimental DC-DC efficiency of proposed WCS. (a) In CC mode. (b) In CV mode. (c) With respect to misalignment in CC mode.

TABLE II
Comparison of Different Exciting WCS With Proposed WCS

	[6],[7]	[9], [10]	[11]	[12],[13]	[14]-[16]	Proposed
Extra DC-DC converter	No	Yes	No	No	No	No
Switching frequency	wide range	fixed	fixed	fixed	fixed	fixed
Reconfigurable tank circuit	No	No	No	No	Yes	No
Size optimization	No	No	No	No	No	Yes
Soft switching	Yes	No	No	No	Yes	Yes
No of coils	2	2	2	2	3	2
Cost	High	High	High	High	High	Low
Complexity	High	High	High	High	High	Low

However, as given by (16), the current gain increases under misalignment. This increase in current gain comes at a cost as the ratio of circuit's reactive power to real power increases more rapidly as shown in Fig. 7(a). In practical case little misalignment may be tolerated by the circuit but if the misalignment is much higher, the ZPA condition may lead to damaging magnitude of circuit currents and some safety mechanism (such as reduction in input voltage) may need to be employed.

Fig. 13(b) shows how V_o, I_o, and P_o in CV mode decreases as the misalignment distance increases. Whenever there is a 5.3 cm misalignment, the output power decreases from 600 W to 241.6 W. Furthermore, in CV charging mode, the reactive power increases as the input phase angle increases with misalignment distance.

Fig. 14(a) and (b) illustrate the variation in V_o and I_o with respect to the change in R_o in the CC and CV modes, respectively. The theoretical efficiency is calculated using the following:

$$\eta = \frac{i_o'^2 R'_o}{i_o'^2 R'_o + I_T^2 R_T + i_o'^2 R_R} = \frac{1}{1 + \frac{R_R}{R'_o} + \frac{R_T R'_o}{(\omega_{cc} M)^2}}. \quad (25)$$

Efficiency plots using SiC (NVH4L075N065SC1) and GaN (IGT60R070D1) devices in CC and CV modes are shown in Fig. 15(a) and (b) respectively. Similarly, the efficiency plot related to misalignment in CC mode is shown in Fig. 15(c).

A comparison of existing systems with the proposed WCS is given in Table II. From the comparison, it is clear that proposed SC-based LLC resonant dc-dc converter offers better performance in term of size and less control complexity.

V. Conclusion

In this letter, a novel SC based *LLC* resonant converter is proposed to achieve CC–CV characteristics at constant switching frequency for EV charging. The system initially works in the CC charging mode using conventional method. The CV charging mode is achieved by using SC network when S_a and S_b are activated. This connects an external capacitor across the compensating capacitors, which reduces the system's resonance frequency by modifying the resonant network. This novel configuration allows for a smooth transition between CC and CV modes while keeping switching frequency to a constant value. Through steady-state analysis, mathematical expressions for current gain, voltage gain, and input impedance are derived. Furthermore, the proposed system is equipped with kVA/kW optimization method for compact design. The system ensures soft switching operation

over the entire load range. The experimental results validate the performance of the proposed WCS. The efficiency improvement of 17% is possible in CC mode by GaN based design compared to the SiC at 100 W.

REFERENCES

[1] A. Ahmad, M. S. Alam, and R. Chabaan, "A comprehensive review of wireless charging technologies for electric vehicles," *IEEE Trans. Transp. Electrific.*, vol. 4, no. 1, pp. 38–63, Mar. 2018.

[2] K. K. Prasad and V. Agarwal, "A comprehensive analysis of single stage wireless power transfer compensation topologies for battery chargers in electric vehicles," in *Proc. IEEE Texas Power Energy Conf.*, 2020, pp. 1–6.

[3] Y. Li, J. Hu, F. Chen, S. Liu, Z. Yan, and Z. He, "A new-variable coil-structure-based IPT system with load-independent constant output current or voltage for charging electric bicycles," *IEEE Trans. Power Electron.*, vol. 33, no. 10, pp. 8226–8230, Oct. 2018.

[4] A. C. Bagchi, A. Kamineni, R. A. Zane, and R. Carlson, "Review and comparative analysis of topologies and control methods in dynamic wireless charging of electric vehicles," *IEEE J. Emerg. Sel. Topics Power Electron.*, vol. 9, no. 4, pp. 4947–4962, Aug. 2021.

[5] M. Kavitha, D. Prasad, and P. B. Bobba, "Methods for overcoming misalignment effects and charging control of a dynamic wireless electric vehicle charging system," *Int. Eng. Technol. Electric Power Appl.*, vol. 13, no. 8, pp. 1184–1192, 2019.

[6] Y.-C. Hsieh, Z.-R. Lin, M.-C. Chen, H.-C. Hsieh, Y.-C. Liu, and H.-J. Chiu, "High-efficiency wireless power transfer system for electric vehicle applications," *IEEE Trans. Circuits Syst.*, vol. 64, no. 8, pp. 942–946, Aug. 2017.

[7] K. Aditya and S. S. Williamson, "Design guidelines to avoid bifurcation in a series–series compensated inductive power transfer system," *IEEE Trans. Ind. Electron.*, vol. 66, no. 5, pp. 3973–3982, May 2019.

[8] *Wireless Power Transfer for Light-Duty plug-in/Electric Vehicles and Alignment Methodology J2954*, SAE Standard J2954_201904, SAE Int., Warrendale, PA, USA, 2019, doi: 10.4271/J2954_201904.

[9] M. Kim, D.-M. Joo, and B. K. Lee, "Design and control of inductive power transfer system for electric vehicles considering wide variation of output voltage and coupling coefficient," *IEEE Trans. Power Electron.*, vol. 34, no. 2, pp. 1197–1208, Feb. 2019.

[10] T.-D. Yeo, D. Kwon, S.-T. Khang, and J.-W. Yu, "Design of maximum efficiency tracking control scheme for closed-loop wireless power charging system employing series resonant tank," *IEEE Trans. Power Electron.*, vol. 32, no. 1, pp. 471–478, Jan. 2017.

[11] K. Song, Z. Li, J. Jiang, and C. Zhu, "Constant current/voltage charging operation for series-series and series-parallel compensated wireless power transfer systems employing primary-side controller," *IEEE Trans. Power Electron.*, vol. 33, no. 9, pp. 8065–8080, Sep. 2018.

[12] S. Liu, X. Li, and L. Yang, "Three-coil structure-based WPT system design for electric bike CC and CV charging without communication," *Int. Eng. Technol. Electric Power Appl.*, vol. 13, no. 9, pp. 1318–1327, Sep. 2019.

[13] Y. Zhang, Z. Shen, W. Pan, H. Wang, Y. Wu, and X. Mao, "Constant current and constant voltage charging of wireless power transfer system based on three-coil structure," *IEEE Trans. Ind. Electron.*, vol. 70, no. 1, pp. 1066–1070, Jan. 2023.

[14] D. Wang, X. Qu, Y. Yao, and P. Yang, "Hybrid inductive-power-transfer battery chargers for electric vehicle onboard charging with configurable charging profile," *IEEE Trans. Intell. Transp. Syst.*, vol. 22, no. 1, pp. 592–599, Jan. 2021.

[15] X. Mao, J. Chen, Y. Zhang, and J. Dong, "A simple and reconfigurable wireless power transfer system with constant voltage and constant current charging," *IEEE Trans. Power Electron.*, vol. 7, no. 5, pp. 4921–4925, May 2022.

[16] D. Wang, C. Fu, X. Bei, and Q. Zhao, "A reconfigurable half-bridge compensation topology-based WPT system with constant current and constant voltage outputs," *IEEE Trans. Circuits Syst. II Exp. Briefs*, vol. 70, no. 1, pp. 256–260, Jan. 2023.